

Supplementary Materials

Three-dimensional MXene coupled CoFe nanoalloys as sulfur host for long-life room-temperature sodium-sulfur batteries

Xiaoming Yu^{1,2}, Hao Li¹, Kuan Liang¹, Shengdong Liu³, Liuqing Li¹, Ye Zhu¹,
Haitao Huang^{1,2,*}

¹Department of Applied Physics, The Hong Kong Polytechnic University, Hong Kong 999077, China.

²The Research Institute for Smart Energy, The Hong Kong Polytechnic University, Hong Kong 999077, China.

³School of Materials and Energy, Guangdong University of Technology, Guangzhou 510006, China.

***Correspondence to:** Prof. Haitao Huang, Department of Applied Physics, The Hong Kong Polytechnic University, Hung Hom, Kowloon, Hong Kong 999077, China.

E-mail: aphhuang@polyu.edu.hk

Computational methods

Within the framework of density functional theory (DFT), all first-principles calculations are conducted using the Vienna Ab initio Simulation Package (VASP)¹. The exchange-correlation functional adopts the generalized gradient approximation (GGA) of Perdew-Burke-Ernzerhof (PBE) form², and the nuclear-electron interaction is described by the projected augmented wave (PAW) pseudopotential³. The kinetic cut-off energy is set at 450 eV. During all the calculations, the energy convergence criterion is specified as 10^{-5} eV, and the force convergence criterion is set at 0.05 eV/Å. In addition, the spin interaction is also considered for each system. The van der Waals interaction is described by the DFT-D3 functional⁴, and a vacuum layer of more than

Energy Materials

15 Å is included in each system to avoid periodic interactions along the z-direction. The k-point mesh for the general models is sampled with a separation of 0.02 \AA^{-1} . Each configuration undergoes full relaxation until meeting the established convergence criteria. The binding energies are calculated using the following formula⁵:

$$E_b = E_{slab+M} - E_{slab} - E_M$$

where E_b is the binding energy of the adsorbed process, E_{slab+M} stands for the total energy of the slab with the adsorbed Na_2S_n , E_{slab} indicates the energy of slab models, and E_M denotes the energy of Na_2S_n . The Gibbs free energy (ΔG) calculations utilized the following formula⁵:

$$\Delta G = E_b + \Delta E_{ZPE} - T\Delta S$$

where the temperature (T) is 298.15 K, while ΔE_{ZPE} and $T\Delta S$ denote the zero point energy difference and entropy difference between the gas phase and the adsorbed phase, respectively.

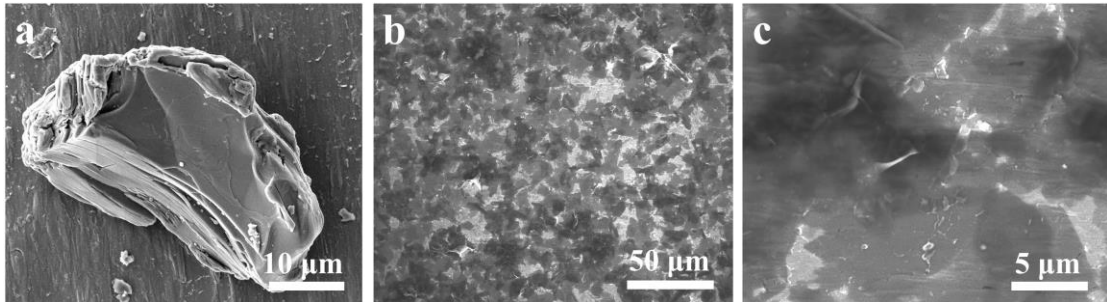


Fig. S1 SEM images of (a) Ti_3AlC_2 MAX and (b) Few-layer $\text{Ti}_3\text{C}_2\text{T}_x$ MXene. (c) Magnified SEM image.

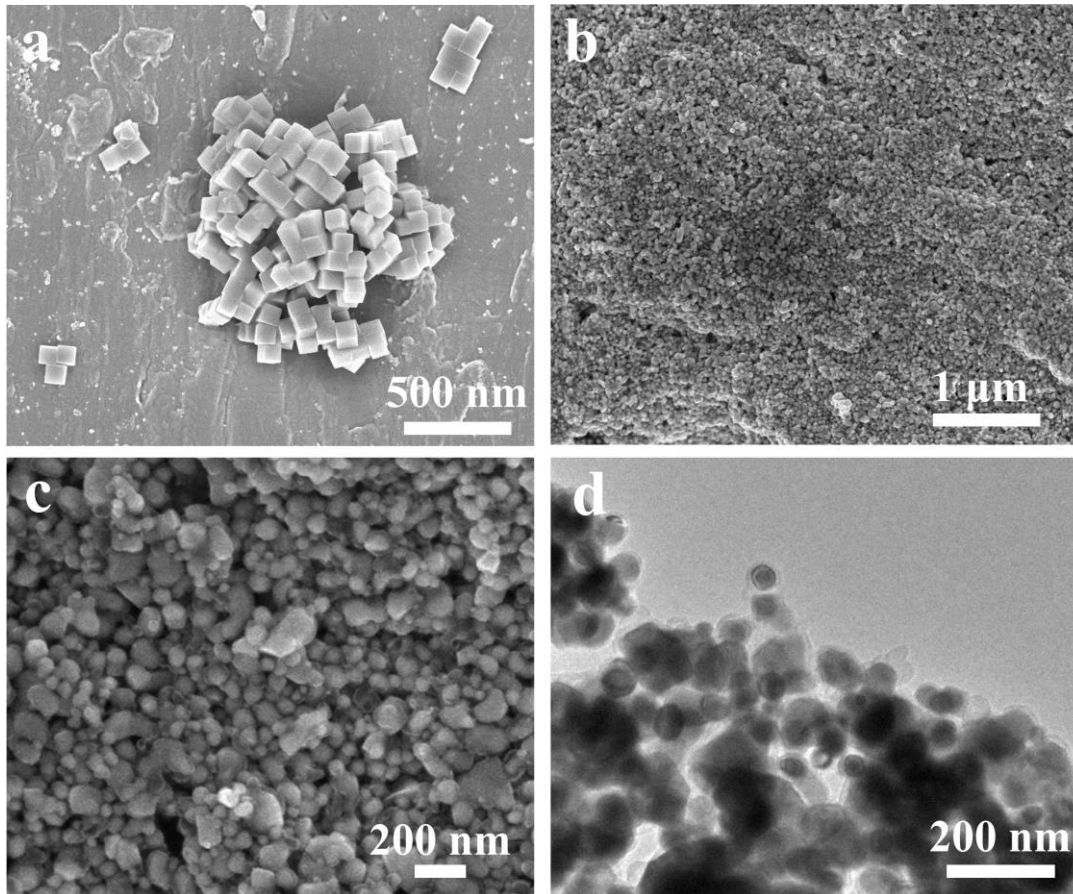


Fig. S2 SEM images of (a) CoFe-PBA and (b) C/CoFe alloy. (c) Magnified SEM image. (d) TEM image.

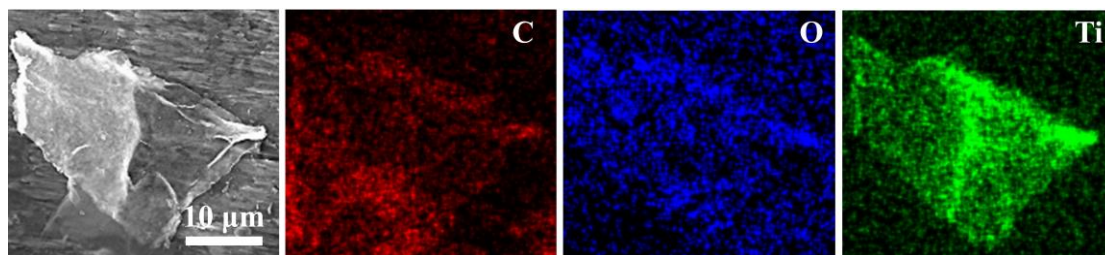


Fig. S3 SEM image and corresponding elemental mapping of few-layer $Ti_3C_2T_x$ MXene.

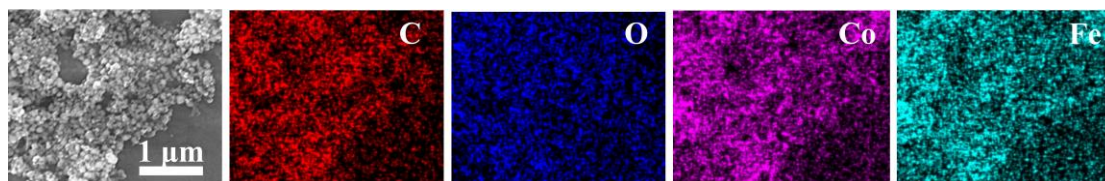


Fig. S4 SEM image and corresponding elemental mapping results of C/CoFe alloy.

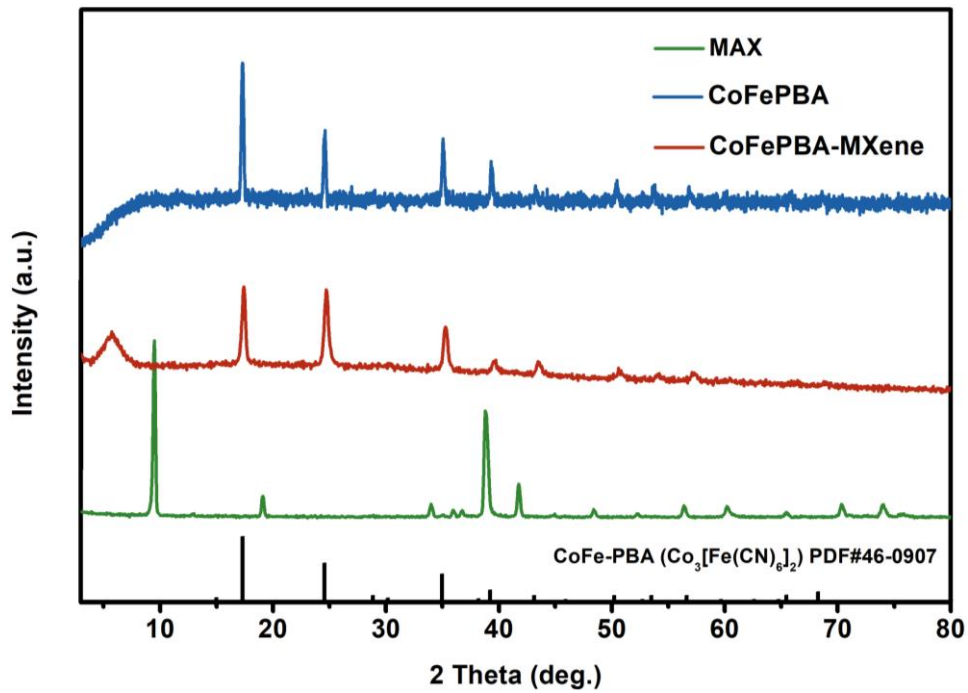


Fig. S5 XRD patterns of MAX, CoFe-PBA and CoFePBA-MXene.

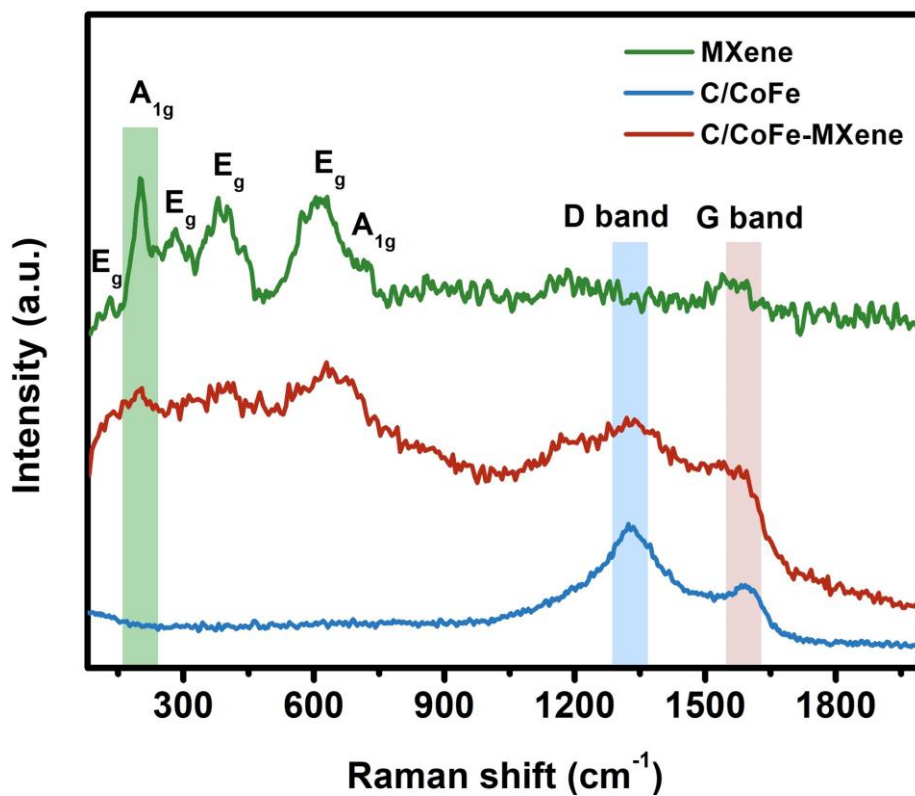


Fig. S6 Raman spectra of MXene, C/CoFe and C/CoFe-MXene.

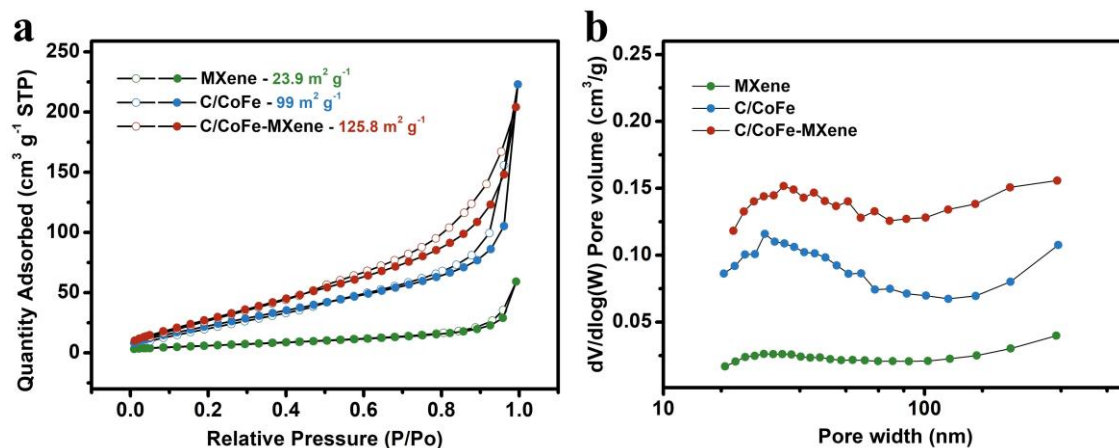


Fig. S7 (a) N_2 adsorption-desorption isotherms and (b) pore width distribution curves of MXene, C/CoFe and C/CoFe-MXene.

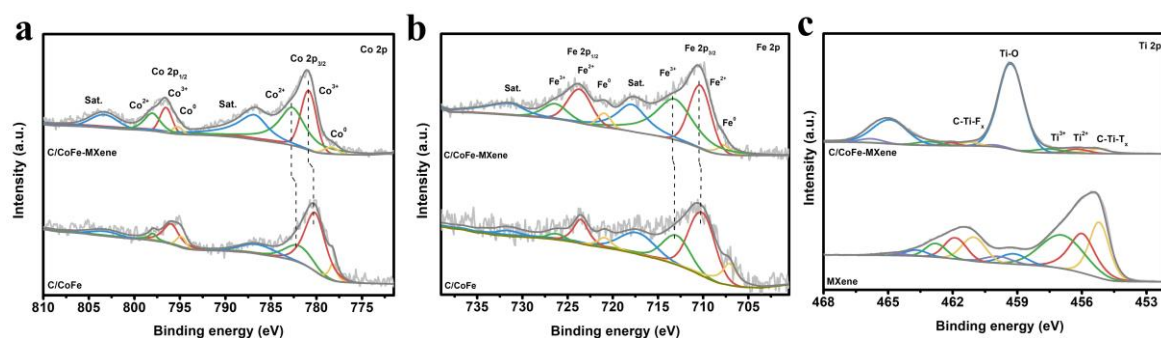


Fig. S8 High resolution XPS spectra of (a) Co 2p, (b) Fe 2p and (c) Ti 2p.

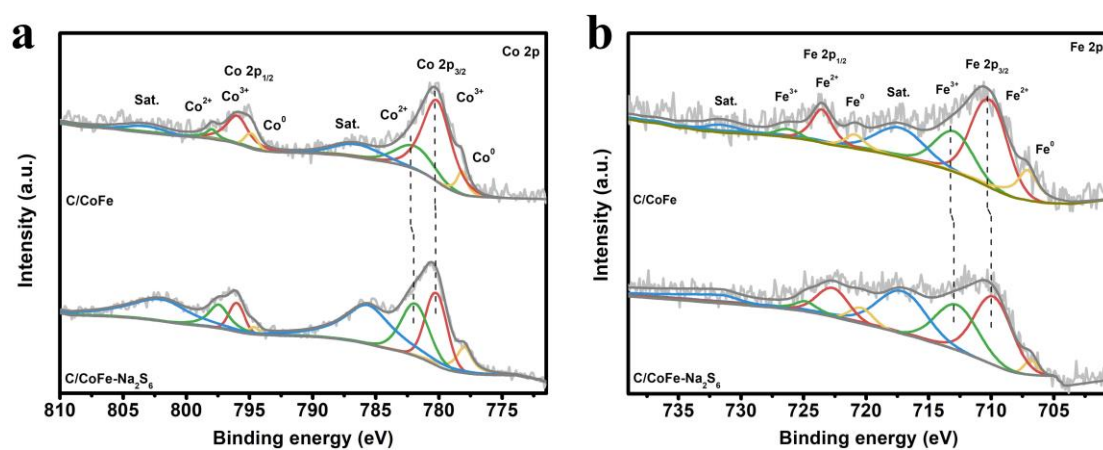


Fig. S9 High resolution XPS spectra of (a) Co 2p and (b) Fe 2p on C/CoFe before and after adsorption.

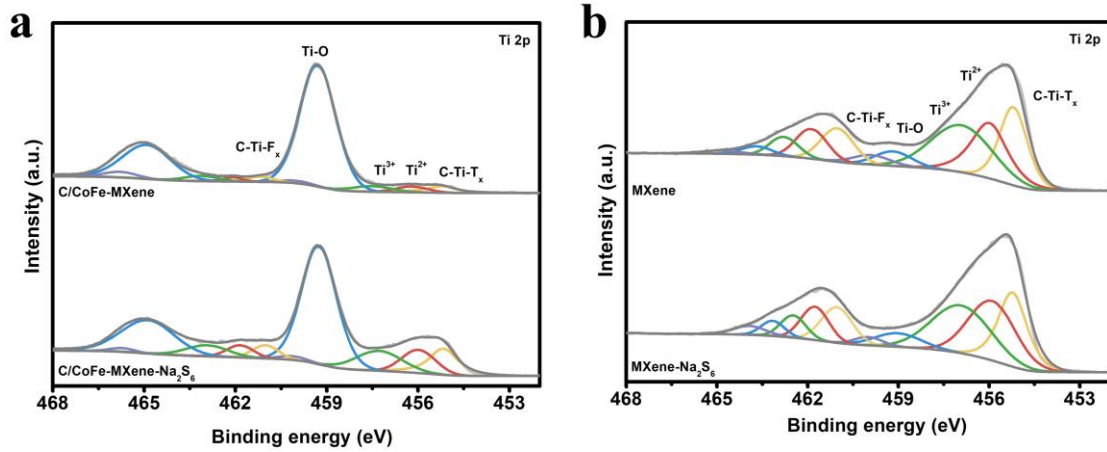


Fig. S10 High resolution XPS spectra of Ti 2p on (a) C/CoFe-MXene, (b) MXene before and after adsorption.

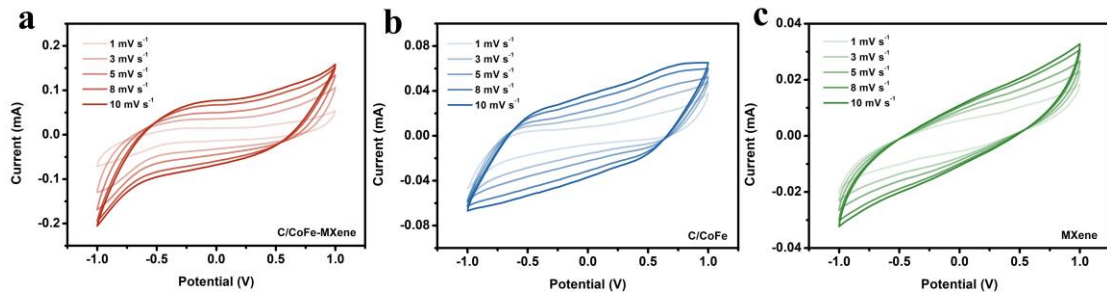


Fig. S11 The symmetric cell with (a) C/CoFe-MXene, (b) C/CoFe and (c) MXene electrodes at scan rates from 1.0 to 10 mV s⁻¹.

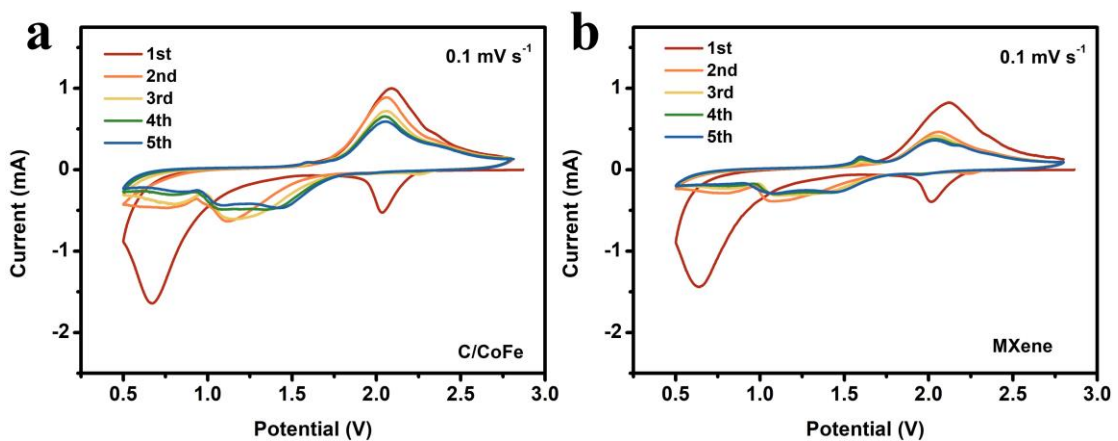


Fig. S12 The first five CV curves of the cell with (a) C/CoFe and (b) MXene electrodes.

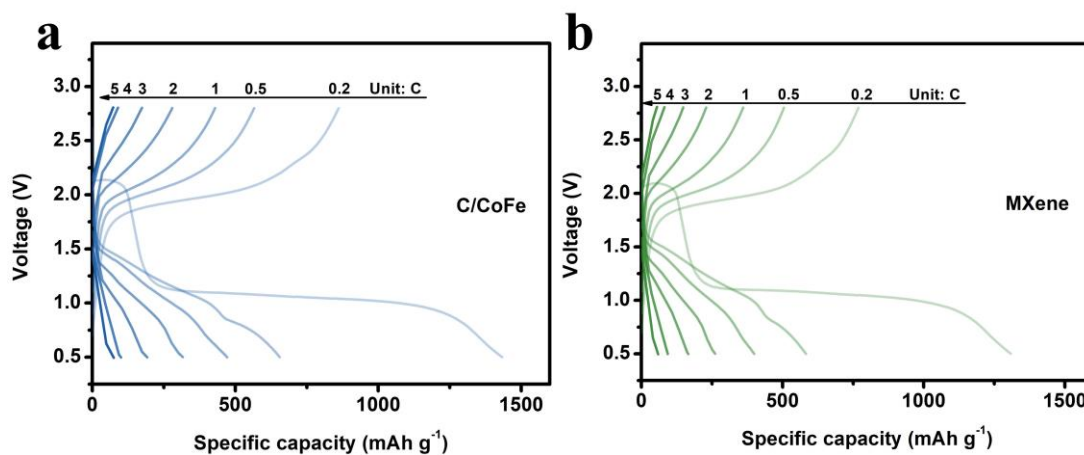


Fig. S13 The galvanostatic charge/discharge profiles of the cells with (a) C/CoFe and (b) MXene electrodes at different rates.

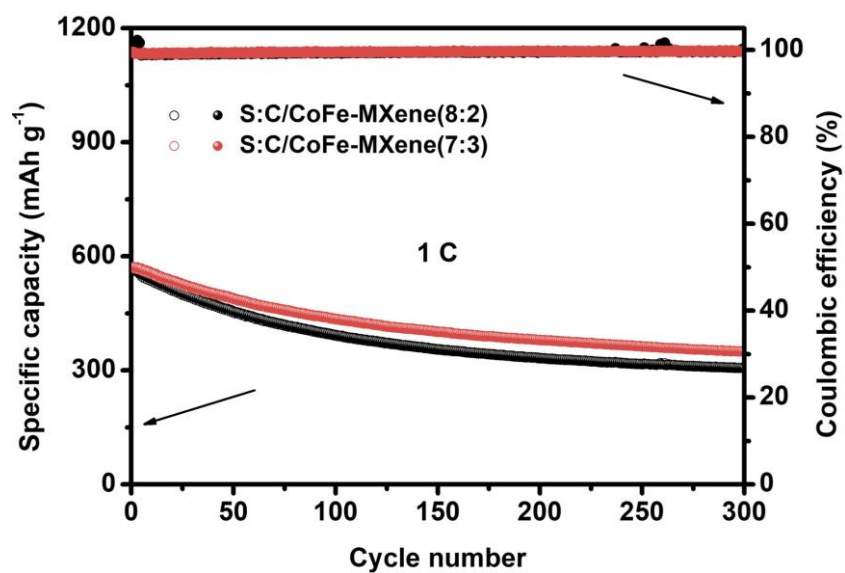


Fig. S14 The cycle performance of the C/CoFe-MXene cathode with different sulfur loading at 1C.

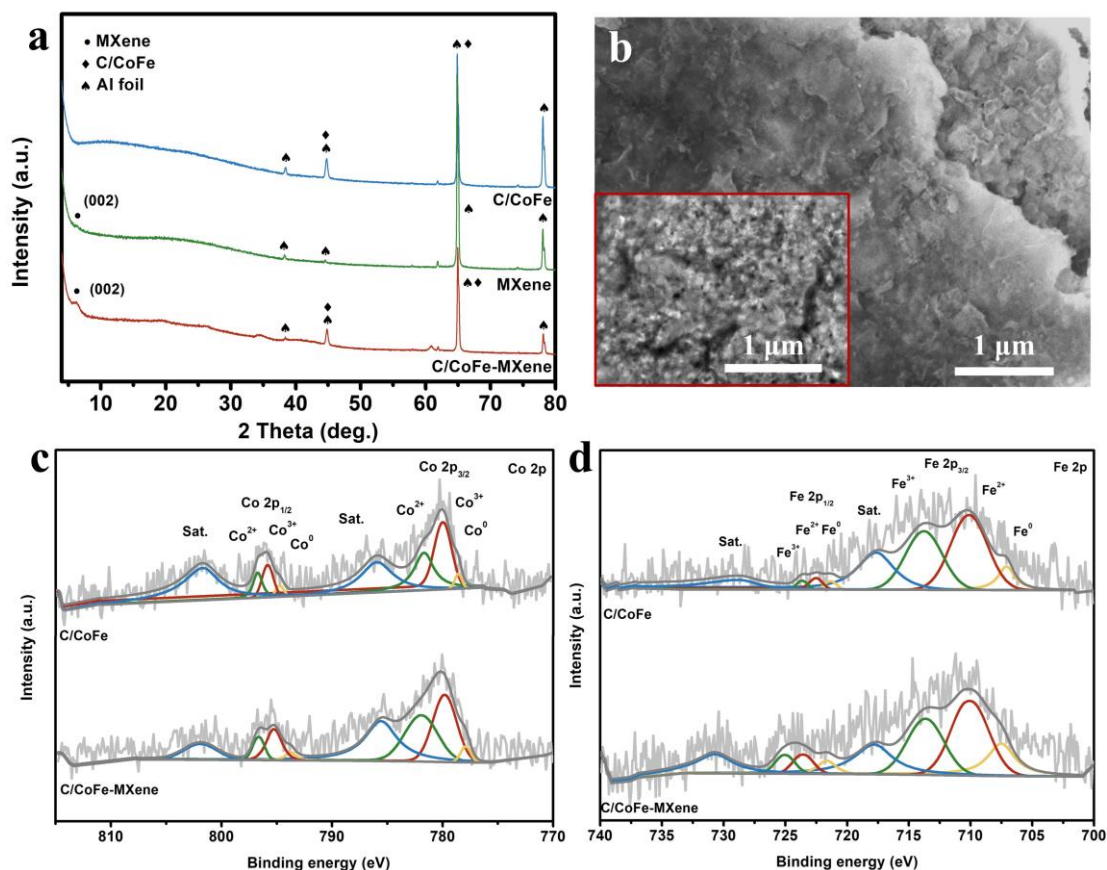


Fig. S15 (a) XRD pattern of C/CoFe-MXene, C/CoFe and MXene electrodes after cycling. (b) SEM images and TEM images (inset) of C/CoFe-MXene after cycling.

High resolution (c) Co 2p, (d) Fe 2p XPS spectrum after cycling.

Firstly, the comparison between cycled MXene and C/CoFe-MXene was conducted. The (002) XRD peak of MXene almost vanished after cycling, implying its great degradation of MXene (Fig. S15a). By contrast, the (002) MXene peak of C/CoFe-MXene nanocomposites only turns broader and the peak position did not change significantly, which indicates the good retention of MXene and its robust interlayer path. These results prove that the incorporated C/CoFe alloy serves as a pillar to prevent MXene from restacking during the long-term cycling and is favorable to the structure stability of C/CoFe-MXene. The cycled C/CoFe and C/CoFe-MXene were then compared. XRD results (Fig. S15a) show that both samples well retain CoFe alloy phase after their cycling and there are no big differences in their XPS results (Fig. S15c-d). It means that the C/CoFe alloy catalyst is relatively stable during cycling. The

Energy Materials

C/CoFe-MXene nanocomposite exhibits a better electrochemical performance than C/CoFe alloy. Thus, one can conclude that MXene is beneficial to the dispersion of the C/CoFe alloy, which makes the C/CoFe alloy catalyzes and adsorbs NaPSs more uniformly and efficiently.

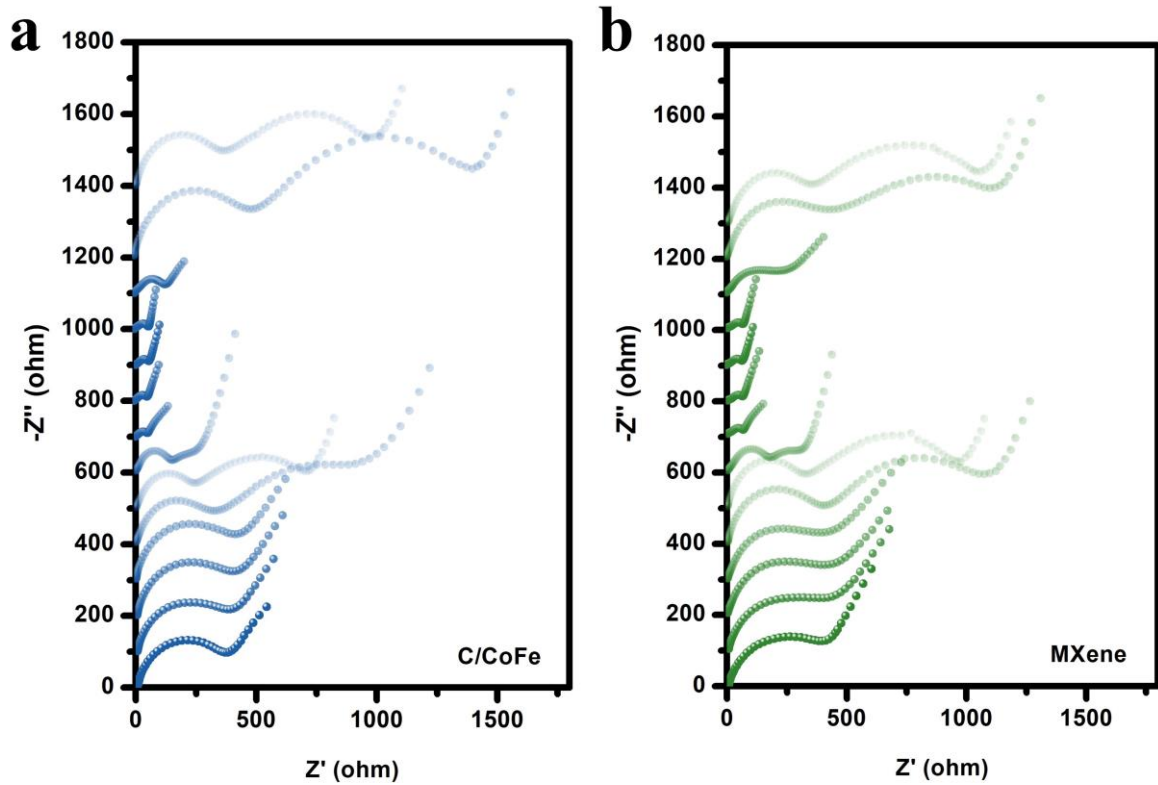


Fig. S16 *In situ* EIS plots of cells with (a) C/CoFe and (b) MXene electrodes at different states

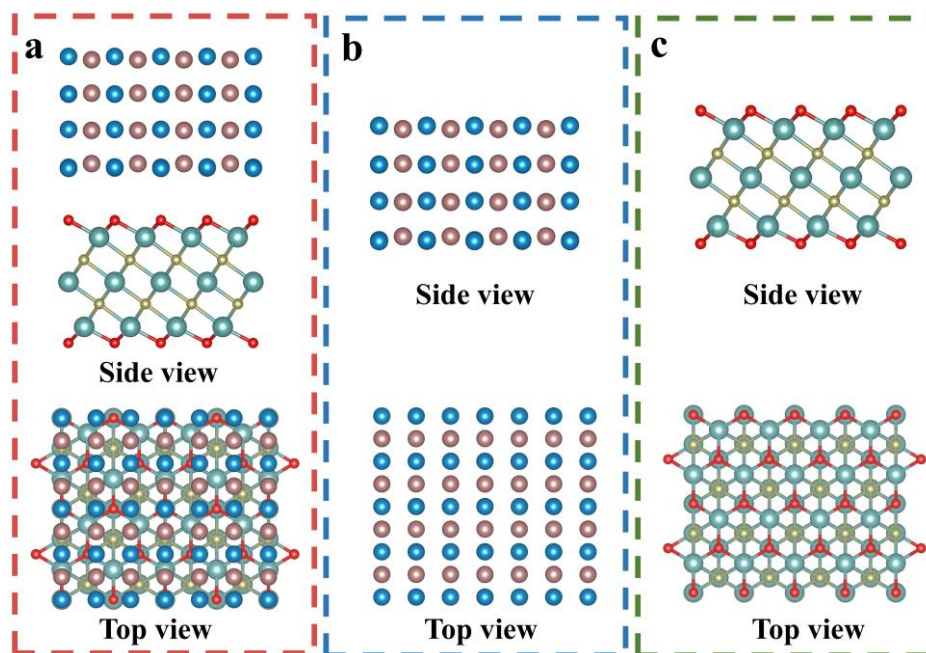


Fig. S17 The optimized atomic configuration of (a) CoFe-MXene, (b) CoFe and (c) MXene.

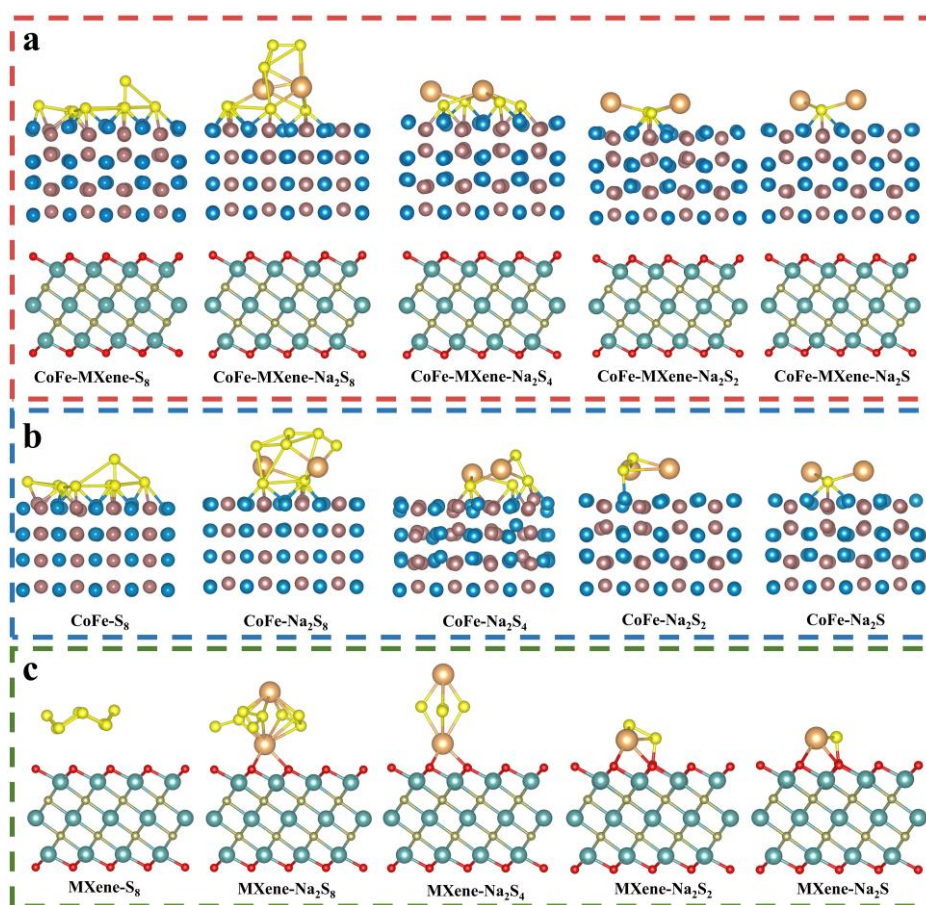


Fig. S18 The optimized adsorption configuration (side view) of (a) CoFe-MXene, (b) CoFe and (c) MXene.

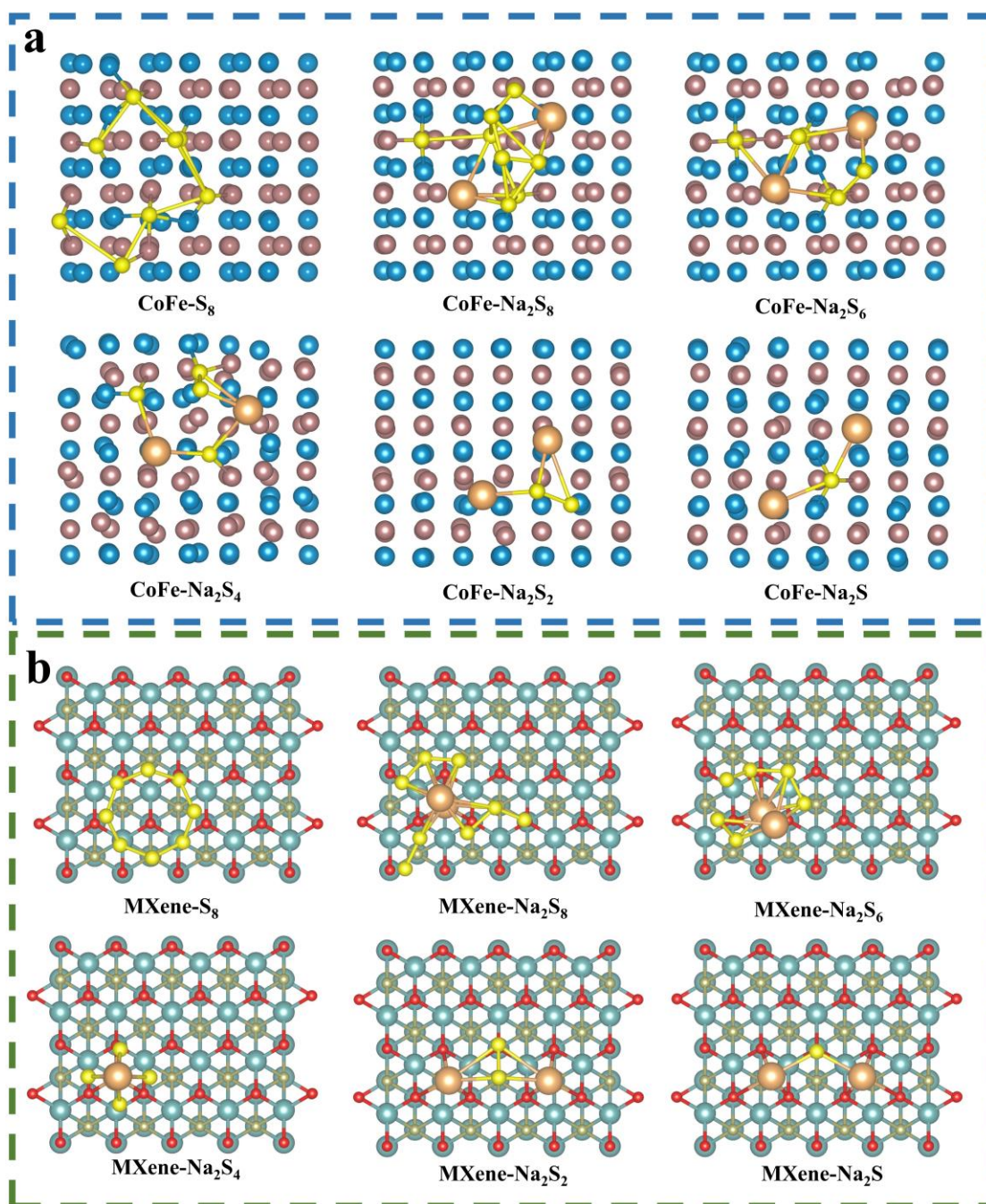


Fig. S19 The optimized adsorption configuration (top view) of (a) CoFe and (b) MXene.

Table S1. Comparison of C/CoFe-MXene with some related work for RT Na-S batteries

Sulfur host	Areal sulfur loading	Specific capacity@1C	Long-term cycle performance	Ref.
C/CoFe-MXene	1.8-2 mg cm ⁻²	572	0.084%@1C (800) 0.00891%@5C (5400)	This work
TiO ₂ -Ti ₃ C ₂	-	650	0.063%@1C (1500)	6
MG-Co	-	495	0.32%@0.5C (200)	7
CNTs/Co@NC	0.7-0.9 mg cm ⁻²	592	0.068%@1C (400)	8
Ni-NCFs	0.5-0.7 mg cm ⁻²	431	0.17%@1C (270)	9
Co@NPCNFs	1 mg cm ⁻²	411	0.038%@1C (800)	10
Co@BNC	0.8-1 mg cm ⁻²	485	0.04%@0.5C (600)	11
Co-CNT/NPC	0.41 mg cm ⁻²	295	0.025%@0.5C (1000)	12
Co/CeO ₂ -NPC	1.5 mg cm ⁻²	600	0.025%@3C (1000)	13
Fe ₁ @NC	-	392	0.032%@0.3C (1320)	14
MoC@NHC-15	2 mg cm ⁻²	513	0.04%@5C (1000)	15

Table S2. Adsorption energies of NaPSs on different samples

	CoFe-MXene (eV)	CoFe (eV)	MXene (eV)
S ₈	-17.71	-17.84	-0.81
Na ₂ S ₈	-19.74	-10.87	-0.90
Na ₂ S ₆	-19.24	-12.71	-1.33
Na ₂ S ₄	-14.13	-8.76	-1.69
Na ₂ S ₂	-9.44	-4.61	-3.79
Na ₂ S	-7.05	-6.99	-3.80

REFERENCE

- [1] Hafner, J. Ab-initio simulations of materials using VASP: Density-functional theory and beyond. *J. Comput. Chem.* **2008**, *29*, 2044-2078, DOI: 10.1002/jcc.21057
- [2] Ernzerhof, M.; Scuseria, G.E. Assessment of the Perdew-Burke-Ernzerhof exchange-correlation functional. *J. Chem. Phys.* **1999**, *110*, 5029-5036, DOI:10.1063/1.478401
- [3] Kresse, G.; Joubert, D. From ultrasoft pseudopotentials to the projector augmented-wave method. *Phys. Rev. B* **1999**, *59*, 1758-1775, DOI:10.1103/PhysRevB.59.1758.
- [4] Grimme, S.; Antony, J.; Ehrlich, S.; Krieg, H. A consistent and accurate ab initio parametrization of density functional dispersion correction (DFT-D) for the 94 elements H-Pu. *J. Chem. Phys.* **2010**, *132*, DOI:10.1063/1.3382344
- [5] Fan, K.; Ying, Y.; Lin, Z.; Tsang, Y.H.; Huang, H. Building up an “Elemental property-adsorption energy descriptor-decomposition barrier” three-tier model for screening biatom catalysts in sodium-sulfur batteries. *Adv. Energy Mater.* **2023**, *13*, 2300871, DOI: 10.1002/aenm.202300871
- [6] Reddy, B.S.; Cho, G.-B.; Reddy, N.S.; Ahn, H.-J.; Ahn, J.-H.; Maiyalagan, T.; Cho, K.-K. Layered-like structure of TiO₂-Ti₃C₂ MXene as an efficient sulfur host for room-temperature sodium-sulfur batteries. *J. Alloys Compd.* **2021**, *883*, 160910, DOI: 10.1016/j.jallcom.2021.160910
- [7] Yang, Q.; Yang, T.; Gao, W.; Qi, Y.; Guo, B.; Zhong, W.; Jiang, J.; Xu, M. An MXene-based aerogel with cobalt nanoparticles as an efficient sulfur host for room-temperature Na-S batteries. *Inorg. Chem. Front.* **2020**, *7*, 4396-4403, DOI:10.1039/D0QI00939C
- [8] Mou, J.; Li, Y.; Liu, T.; Zhang, W.; Li, M.; Xu, Y.; Zhong, L.; Pan, W.; Yang, C.; Huang, J. Metal-Organic Frameworks-Derived Nitrogen-Doped Porous Carbon Nanocubes with Embedded Co Nanoparticles as Efficient Sulfur Immobilizers for Room Temperature Sodium-Sulfur Batteries. *Small Methods* **2021**, *5*, 2100455, DOI: 10.1002/smt.202100455
- [9] Guo, B.; Du, W.; Yang, T.; Deng, J.; Liu, D.; Qi, Y.; Jiang, J.; Bao, S.-J.; Xu, M. Nickel Hollow Spheres Concatenated by Nitrogen-Doped Carbon Fibers for Enhancing Electrochemical Kinetics of Sodium-Sulfur Batteries. *Adv. Sci.* **2020**, *7*, 1902617, DOI:

10.1002/advs.201902617

- [10] Du, W.; Gao, W.; Yang, T.; Guo, B.; Zhang, L.; Bao, S.-j.; Chen, Y.; Xu, M. Cobalt nanoparticles embedded into free-standing carbon nanofibers as catalyst for room-temperature sodium-sulfur batteries. *J. Colloid Interface Sci.* **2020**, *565*, 63-69, DOI: 10.1016/j.jcis.2020.01.010
- [11] Tang, K.; Peng, X.; Zhang, Z.; Li, G.; Wang, J.; Wang, Y.; Chen, C.; Zhang, N.; Xie, X.; Wu, Z. A Highly Dispersed Cobalt Electrocatalyst with Electron-Deficient Centers Induced by Boron toward Enhanced Adsorption and Electrocatalysis for Room-Temperature Sodium-Sulfur Batteries. *Small* **2024**, *20*, 2311151, DOI: 10.1002/sml.202311151
- [12] Liu, H.; Wu, Y.; Liu, P.; Wang, H.; Xu, M.; Bao, S.-j. Anthozoan-like porous nanocages with nano-cobalt-armed CNT multifunctional layers as a cathode material for highly stable Na-S batteries. *Inorg. Chem. Front.* **2022**, *9*, 645-651, DOI:10.1039/D1QI01406D.
- [13] Ou, L.; Mou, J.; Peng, J.; Zhang, Y.; Chen, Y.; Huang, J. Heterostructured Co/CeO₂-Decorating N-Doped Porous Carbon Nanocubes as Efficient Sulfur Hosts with Enhanced Rate Capability and Cycling Durability toward Room-Temperature Na-S Batteries. *ACS Appl. Mater. Interfaces* **2024**, *16*, 3302-3310, DOI:10.1021/acsami.3c14578
- [14] Lai, W.-H.; Wang, H.; Zheng, L.; Jiang, Q.; Yan, Z.-C.; Wang, L.; Yoshikawa, H.; Matsumura, D.; Sun, Q.; Wang, Y.-X. General Synthesis of Single-Atom Catalysts for Hydrogen Evolution Reactions and Room-Temperature Na-S Batteries. *Angew. Chem. Int. Ed.* **2020**, *59*, 22171-22178, DOI: 10.1002/anie.202009400
- [15] Mou, J.; Li, Y.; Ou, L.; Huang, J. A highly-efficient electrocatalyst for room temperature sodium-sulfur batteries: assembled nitrogen-doped hollow porous carbon spheres decorated with ultrafine α -MoC_{1-x} nanoparticles. *Energy Stor. Mater.* **2022**, *52*, 111-119, DOI: 10.1016/j.ensm.2022.07.028